Hortelao, AC; Simó, C; Guix, M; Guallar-Garrido, S; Julián, E; Vilela, D; Rejc, L; Ramos-Cabrer, P; Cossío, U; Gómez-Vallejo, V; Patiño, T; Llop, J; Sánchez, S. Swarming behavior and in vivo monitoring of enzymatic nanomotors within the bladder, Sci. Robot., 6 (52) 2021

This is the author's version of the work. It is posted here by permission of the AAAS for personal use, not for redistribution. The definitive version was published in Science Robotics on Volume 6 17/03/2021, DOI: 10.1126/scirobotics.abd2823

Swarming behavior and in vivo monitoring of enzymatic nanomotors within the bladder

Ana C. HortelaoDiana Vilela[11], Luka Rejc[,5‡], Jordi Llop[1]*, Cristina Simó[2†], Pedro Ramos-Cabrer[2‡], Samuel Sánchez[2]*, Maria Guix[1][1,6‡], Sandra Guallar-Garrido[2,4], Unai Cossío[2], Vanessa Gómez-Vallejo[3], Esther Julián[3], [2]Tania Patiño

Enzyme-powered nanomotors are an exciting technology for biomedical applications due to their ability to navigate within biological environments using endogenous fuels. However, limited studies into their collective behavior and demonstrations of tracking enzyme nanomotors in vivo have hindered progress toward their clinical translation. Here, we report the swarming behavior of urease-powered nanomotors and its tracking using positron emission tomography (PET), both in vitro and in vivo. For that, mesoporous silica nanoparticles containing urease enzymes and gold nanoparticles were used as nanomotors. To image them, nanomotors were radiolabeled with ^{124}I on gold nanoparticles or ^{18}F-labeled prosthetic group to urease. In vitro experiments showed enhanced

either

fluid mixing and collective migration of nanomotors, demonstrating higher capability to swim across complex paths inside microfabricated phantoms, compared with inactive nanomotors. In vivo intravenous administration in mice confirmed their biocompatibility at the administered dose and the suitability of PET to quantitatively track nanomotors in vivo. Furthermore, nanomotors were administered directly into the bladder of mice by intravesical injection. When injected with the fuel, urea, a homogeneous distribution was observed even after the entrance of fresh urine. By contrast, control experiments using nonmotile nanomotors (i.e., without fuel or without urease) resulted in sustained phase separation, indicating that the nanomotors' self-propulsion promotes convection and mixing in living reservoirs. Active collective dynamics, together with the medical imaging tracking, constitute a key milestone and a step forward in the field of biomedical nanorobotics, paving the way toward their use in theranostic applications.

INTRODUCTION

Self-propelled particles hold potential to overcome the biological barriers that limit current cancer nanomedicines, where only 0.7% of the administered dose reaches the target in vivo (*1*). In this regard, micro- and nanomotors have demonstrated enhanced targeting properties (*2*–*5*) and superior drug delivery efficiency compared with passive particles (*6*–*9*). In addition, they outperform traditional nanoparticles in terms of penetration into biological material, such as mucus (*10*–*13*), cells (*14*–*16*), or spheroids (*4*, *17*). Using enzymes as biocatalysts is emerging as a particularly elegant approach when designing self-propelled particles, due to the use of endogenous fuels, which enables nanomotors' on-site activation and the design of fully biocompatible motor-fuel complexes. Moreover, the library of enzyme/substrate combinations permits the design of application- tailored enzymatic nanomotors, as is the case of urease-powered nanomotors for bladder cancer therapy (*4*).

Yet, the large number of nanoparticles required to treat tumors (*18*) demands better understanding, control, and visualization of nanoparticle swarms to aid in the evaluation of motile nanomedicines and facilitate the eventual translation into clinics. Collective phenomena commonly observed in nature [active filaments (*19*); bacteria quorum sensing (*20*); cell migration (*21*); and swarms of fish, ants, and birds (*22*)] also occur in micro/nanomotors, which have demonstrated collective migration (*23*–*26*), assembly (*27*–*30*), and aggregation/ diffusion behaviors in vitro (*31*–*38*). Ex vivo, swarms of magnetic micropropellers have displayed long-range propulsion through porcine eyes to the retina, suggesting potential as active ocular delivery devices (*39*, *40*). In vivo, controlled swimming of micromotor swarms has been observed in mouse peritoneal cavities (*41*), and micromotor swarms have been tracked in the stomach (*24*) and intestines (*26*) of rodents using magnetic resonance imaging and photoacoustic computed tomography, respectively. The sensitivity of these imaging techniques, however, is too low, and they fail to provide quantitative information.

Positron emission tomography (PET), a noninvasive nuclear imaging technique widely used in clinics, offers certain key advantages to address the aforementioned limitations. First, it is fully quantitative and allows whole-body image acquisition. Second, it relies on gamma-ray detection, which has no tissue-penetration limit, turning this imaging modality into a fully translational tool. Last, it is extremely sensitive, thus providing high-quality images by administering subpharmacological dosages of the radiolabeled

---

[1]Institute for Bioengineering of Catalonia (IBEC), Barcelona Institute of Science and Technology (BIST), Baldiri i Reixac 10-12, 08028 Barcelona Spain. [2]CIC biomaGUNE, Basque Research and Technology Alliance (BRTA), 20014 San Sebastian, Guipúzcoa,Spain. [3]Departament de Genètica i de Microbiologia, Facultat de Biociències Universitat Autònoma de Barcelona, 08193 Bellaterra, Barcelona, Spain. [4]Ikerbasque Basque Foundation for Science, Bilbao 48009, Spain. [5]Chemistry Department, University of Rome, Tor Vergata, Via della Ricerca Scientifica, 00133 Rome, Italy, [6]Institució Catalana de Recerca i Estudis Avancats (ICREA), Passeig Lluís Companys 23, 08010 Barcelona, Spain.

*These authors contributed equally to this work.†Present address: University of Ljubljana, Faculty of Chemistry and Chemical Technology, Večna pot 113, 1000 Ljubljana, Slovenia.‡Corresponding author. Email: jllop@cicbiomagune.es (J.L.); ssanchez@ibecbarcelona.eu (S.S.); tpatino@ibecbarcelona.eu (T.P.)

entity (*42*, *43*). Unexpectedly, its application for in vivo tracking of micro/ nanomotors has barely been explored (*44*).

Here, we investigate the swarm behavior of enzyme-powered nanomotors in vitro and in vivo, using PET in combination with computed tomography (CT). We prepared enzyme-powered nanomotors based on a mesoporous silica chassis and labeled them with iodine-124 (^{124}I; half-life = 4.2 days) and fluorine-18 (^{18}F; half-life = 119.7 min). The suitability of PET imaging to investigate the swarm behavior of labeled nanomotors in the presence of the fuel was first demonstrated in vitro using tailored phantoms. Stability of the label and whole-body biodistribution were then investigated in vivo after intravenous administration into mice. Last, time-resolved evidence of the motile properties of the nanomotors in the bladder was obtained after intravesical instillation.

RESULTS

Nanomotors were prepared by synthesizing mesoporous silica nanoparticles (MSNPs) using a modification of the Stöber method (see experimental section for details) (*45*), and their surface was modified with amine groups by attaching aminopropyltriethoxysilane (APTES) (*46*). The amine groups were subsequently activated with glutaraldehyde (GA) to enable the covalent binding of the enzymes and the heterobifunctional polyethylene glycol (NH_2-PEG-SH). Last, gold nanoparticles (AuNPs) were anchored to the surface of the nanomotors by attachment to NH_2-PEG-SH via thiol-gold chemistry (Fig. 1A).

The hydrodynamic radii and stability of nanoparticles along the different fabrication steps were monitored by dynamic light scattering (DLS) analysis. The single population peak corresponding to MSNPs became sharper upon addition of NH_2-PEG-SH, suggesting that PEG provides steric stabilization to the nanomotors in solution (*47*). The single population peak was conserved after attachment of AuNPs, confirming that the final synthetic step of the process did not induce aggregation.

Electrophoretic mobility analysis was performed to characterize the surface properties of the particles after each functionalization step.

Z-potential values for MSNP-NH_2 were found to be 37.1 ± 1.4 mV. The trend toward a negatively charged surface in subsequent synthetic steps confirms the successful activation of the MSNP-NH_2 with GA (*Z*-potential = −2.2 ± 0.2 mV) and incorporation of NH_2PEG-SH and urease enzymes (*Z*-potential = −32.0 ± 0.6 mV). The final negative value can be explained by urease's isoelectric point (~5), such that at pH > 5, the net charge of urease is negative, and by the negative charge of the AuNPs (*48*). The spherical nanoparticles had an average diameter of 507.8 ± 3.4 nm and a stochastic distribution of the AuNPs on the surface, as shown in the transmission electron microscopy (TEM) image (Fig. 1B and fig. S1).

Next, to enable the visualization of the nanomotors by PET, we radiolabeled them with the positron emitters ^{18}F and ^{124}I (Fig. 1C). For the radiofluorination, a straightforward strategy based on the use of the prelabeled prosthetic group 6-[^{18}F]fluoronicotinic acid 2,3,5,6-tetrafluorophenyl ester ([^{18}F]F-PyTFP) was developed (*49*). Taking advantage of the free amino groups on the enzyme, sufficient labeling yield (30% with respect to [^{18}F]F-PyTFP, decay corrected) was achieved by incubation (35 min at room temperature) of the nanomotors with the prosthetic group. Radioiodination was achieved by direct absorption of ^{124}I on AuNPs on the nanomotors (*50*). The radiochemical yield was 71 ± 2%, due to the high-affinity binding between gold and iodine. Radiochemical purity after purification was ≥99% for both cases, as determined by instant thin layer chromatography (Fig. 1D).

The self-propulsion of urease-modified micro/nanomotors (*4*, *51–53*) is caused by the asymmetric release of ionic species from the particles to the solution (*54*), which stems from the catalytic decomposition of urea into carbon dioxide and ammonia (fig. S2 and movie S1). Despite the recent advances in the field, enzyme nanomotors have only been studied from a single-particle point of view and, in some cases, a few particles. However, their collective swarming behavior has yet to be investigated.

The motion dynamics and swarming behavior of nanomotors in vitro were first investigated by optical microscopy. A 2-μl droplet of nanomotors suspension was placed onto a petri dish containing either pure water or 300 mM urea water (urea concentration was chosen on the basis of a known upper limit concentration in the bladder) (*55*), and videos were recorded over 2 min (Fig. 2, A and B; figs. S3 and S4; and movie S2). Figure 2A suggests that after addition of the droplet in water, the nanomotors mainly stayed at the seeding point following a stochastic distribution, which remained unaltered over time as observed in the histograms of pixel intensity distributions obtained for the selected region of interest (ROI) (Fig. 2C). Preferential tracks were observed immediately after seeding due to the motion of the nanomotors in urea, resulting in an anisotropic distribution of the nanomotors throughout the dish. This distribution also evolved over time, as observed in Fig. 2B and evidenced by the dynamic changes in the histograms (Fig. 2D). The same experiment was performed using phosphate-buffered saline (PBS) as solvent, yielding similar results (figs. S5 to S7 and movie S3). Moreover, we studied the nanomotor swarming phenomena by incorporating tracer particles into the system. For this, we codropped 5-μm polystyrene (PS) particles with the nanomotors into the petri dish and monitored the PS tracers' behavior. We observed that when dropped in water or PBS, the swarms and tracers did not exhibit any displacement. However, in the presence of 300 mM urea, the nanomotors exhibited collective motion, dragging along the PS tracers, as evidenced by their trajectories (figs. S9 and S10). This was also denoted in the parabolic shape of the mean-squared displacement of the tracers, indicating their effective displacement.

To gain further insight into swarm dynamics, we then generated density maps. These were obtained by representing sum pixel intensity values of video frames within preestablished time ranges (0 to 40 s, 40 to 80 s, and 80 to 120 s) using a color map (Fig. 2E and figs. S3 to S5 and S7). In absence of urea, density maps did not substantially vary with time, and pixel intensity values for most of the population were around 60 (Fig. 2E, top). On the other hand, the density maps for nanomotors in urea show multiple paths followed by the nanomotors immediately after droplet addition (Fig. 2E, bottom). This is shown as a fast change in the color of the density maps, where the intensity of the overall field of view and nanomotor flocks rapidly increase, indicating high mobility and low residence time.

To investigate whether the activity of the nanomotors and the swarming behavior were associated with fluid flow generation, we

Fig. 1. Preparation and characterization of radiolabeled urease-powered, AuNP-decorated nanomotors. (**A**) Process flow of nanomotors fabrication steps. (**B**) Characterization of the nanomotors by DLS, *Z*-potential, and TEM. (**C**) Nanomotors radiolabeling using either ^{18}F or ^{124}I to yield ^{18}F-nanomotors or ^{124}I-nanomotors, respectively. (**D**) Labeling efficiency and radiochemical purity monitored by iTLC

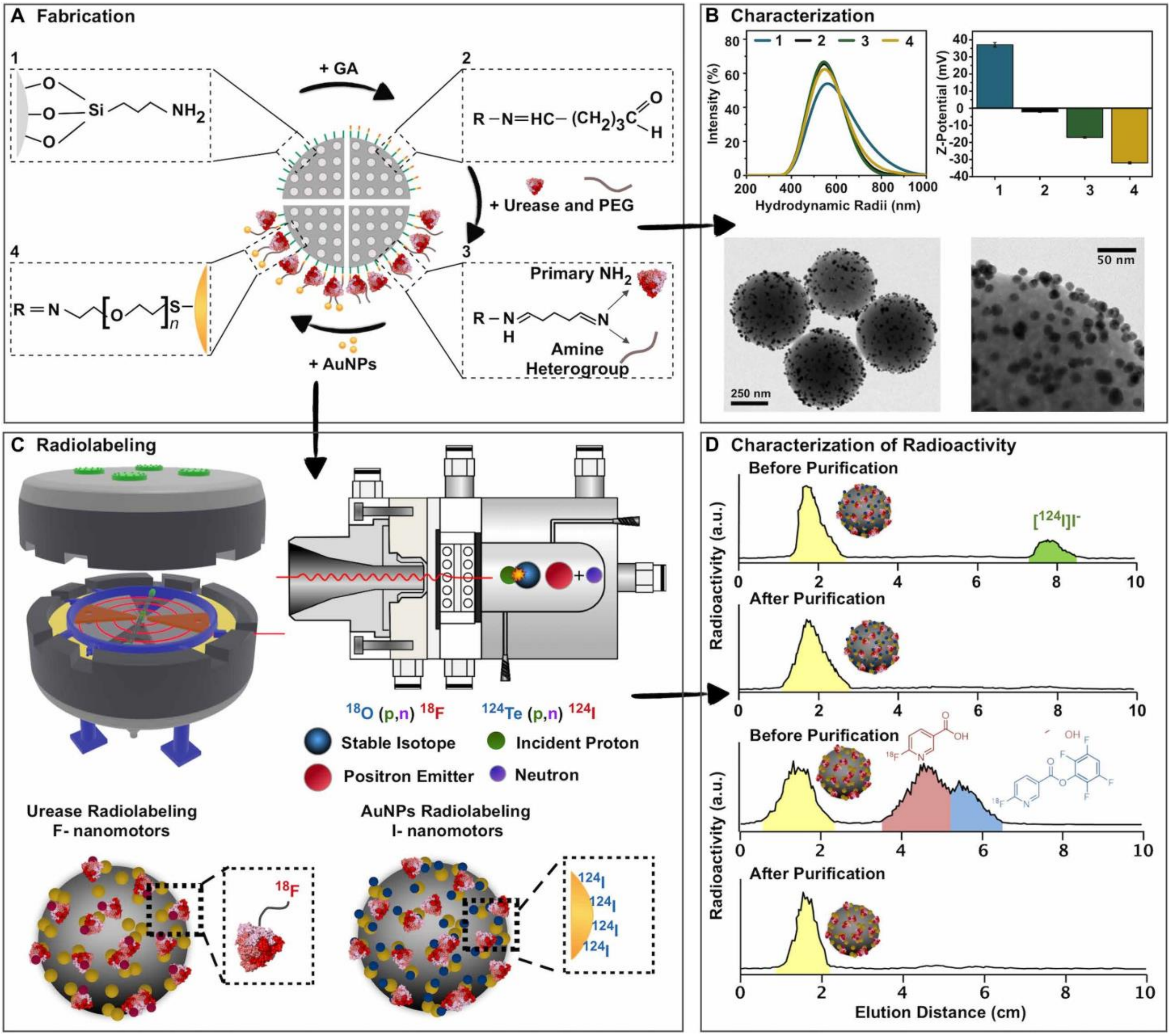

A Fabrication
1
Si
NH2
+ GA
2
R−N=HC−(CH2)3C(=O)H
+ Urease and PEG
3
Primary NH2
R−NH
N
Amine Heterogroup
4
R=N
O
S−
n
+ AuNPs
B Characterization
1 2 3 4
Intensity (%)
80
60
40
20
0
200 400 600 800 1000
Hydrodynamic Radii (nm)
Z-Potential (mV)
40 30 20 10 0 -10 -20 -30 -40
1 2 3 4
50 nm
250 nm
C Radiolabeling
18O (p,n) 18F
124Te (p,n) 124I
Stable Isotope
Incident Proton
Positron Emitter
Neutron
Urease Radiolabeling F- nanomotors
AuNPs Radiolabeling I- nanomotors
18F
124I
124I
124I
124I
D Characterization of Radioactivity
Before Purification
[124I]I-
Radioactivity (a.u.)
0 2 4 6 8 10
After Purification
0 2 4 6 8 10
Before Purification
Radioactivity (a.u.)
0 2 4 6 8 10
After Purification
0 2 4 6 8 10
Elution Distance (cm)

carried out particle image velocimetry (PIV) analyses on the optical microscopy videos (Fig. 2E, inserts). PIV is an optical technique that allows the visualization of fluid flow associated with particle motility, indicating fluid and particle displacements in the form of vector fields. Under the control condition (Fig. 2E, top), the quiver plots show velocity vectors with low magnitude and in scarce amount (small panels). Conversely, the quiver plots obtained for nanomotors in urea show dispersed vector fields emerging not only from the swarms but also from the surrounding fluid. The evolution of the vector fields in time denotes the formation of vortices and fronts that promptly dissociate. Together, these results demonstrate that the activity of the nanomotors and their emergent collective behavior induce enhanced convection and fluid mixing, similar to what has been observed with catalytic micromotors (*56*–*58*). We hypothesize that these convective fluid flows arise from differences in the densities of enzymes' substrates and products, in a similar manner to that observed enzymatic micropumps (*59*–*62*).

To corroborate these results and assess the feasibility of PET imaging to track swarm dynamics, we carried out parallel experiments with radiolabeled nanomotors. PET images obtained at different times after droplet addition confirmed that the nanomotors remained at the seeding point in water (Fig. 3A) and uniformly distributed over the whole volume of the petri dish in the presence of urea (Fig. 3B and movie S6). This behavior could also be visualized in three-dimensional (3D) histograms, which represent the concentration of radioactivity throughout the petri dish (Fig. 3, C and D). Overall, these experiments demonstrated the suitability of

PET imaging to obtain time-resolved quantitative information about the nanomotor swarming dynamics in vitro.

The in vitro swarming behavior of the nanomotors was investigated in four polydimethylsiloxane phantoms with increasing degrees of complexity (Fig. 4, A (top) and B to E, and fig. S11). The selected phantoms comprise different path shapes: (i) straight, (ii) rectangular, (iii) curved, and (iv) a curved path with longer straight trenches. Phantoms were positioned horizontally, and in each phantom, one channel was filled with water and another channel with 300 mM urea solution in water. The nanomotors (either ^{124}I- or ^{18}F-labeled) were seeded at the edge of each channel, and dynamic PET images were immediately acquired for 25 min.

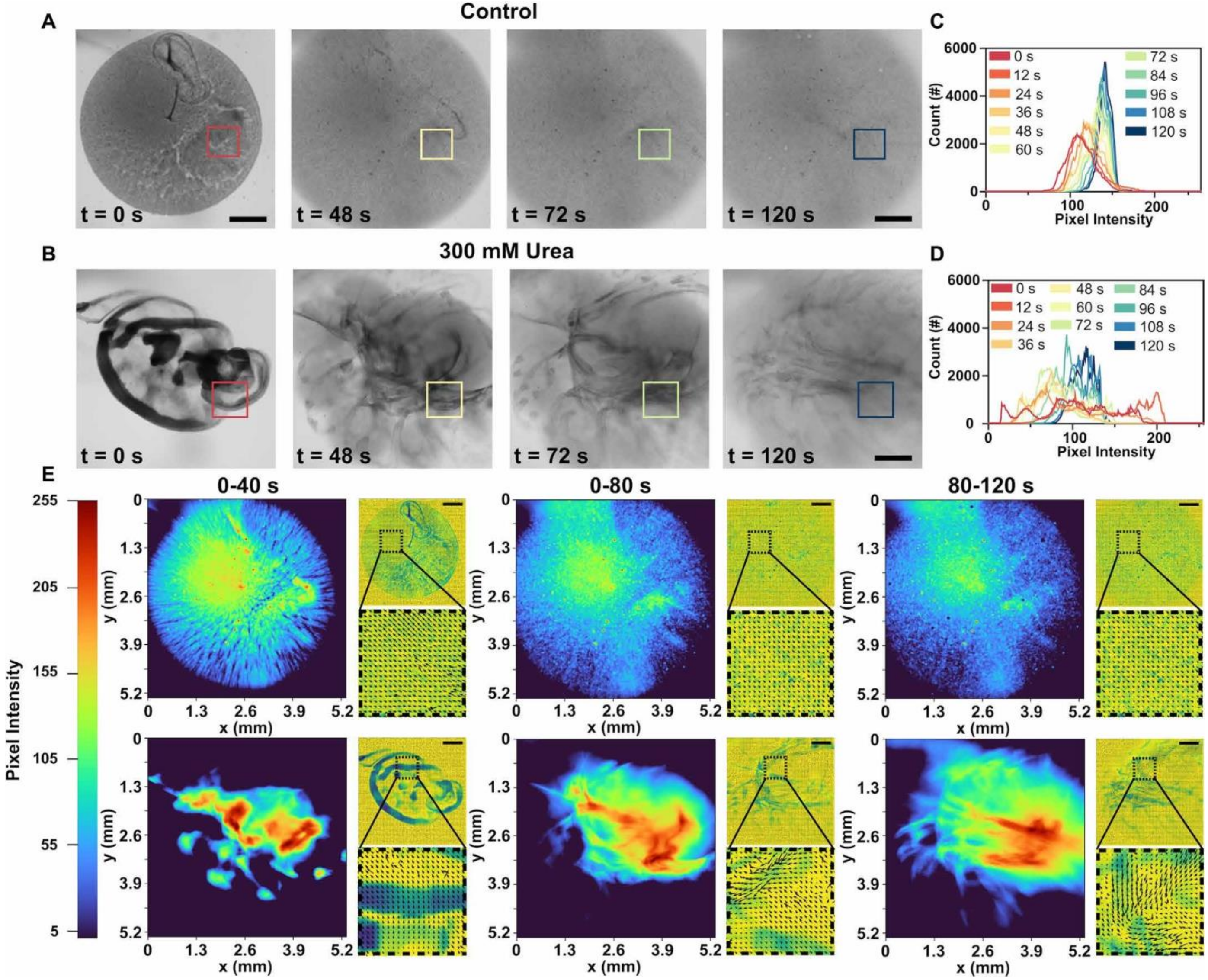

Fig. 2. In vitro imaging of urease-powered nanomotor swarms by optical microscopy. Snapshots of a population of urease-powered nanomotors in (**A**) water and (**B**) 300 mM urea in water. Scale bar, 1 mm. Corresponding pixel intensity distribution histograms within the ROIs noted in the images of nanomotors in (**C**) water and (**D**) 300 mM urea in water. Density maps (large panels) obtained by calculating the sum pixel intensity over periods of 40 s of the videos and PIV (small panels and zoom out) of (**E**) nanomotors in water (top) and in 300 mM urea in water (bottom); scale bar in small panels, 1 mm.

The images obtained at *t* = 0.5, 7, and 25 min after seeding the ^{18}F-nanomotors (Fig. 4, B and E, and movie S7) show that urea has a prominent effect on the motion dynamics of the nanomotors throughout the paths. Irrespective of the path shape, the nanomotors reached the end of the channel at *t* = 25 min in the presence of the fuel, whereas most nanomotors remained close to the seeding point in water, where only minimal movement could be detected.

To get quantitative data, dynamic PET images were analyzed by dividing the phantoms in sectors (Fig. 4A, bottom right), and the concentration of radioactivity in each sector (normalized to the total amount of radioactivity in the channel) was determined as a function of time. Differences were evident even in the less restrictive phantom (straight shape), in which free diffusion of nonactivated nanomotors is more favored. Curves with higher slope were obtained in sectors A to D in urea (Fig. 4B), confirming that the speed at which the nanomotors reach the different sectors is higher than in water. In addition, the fraction of nanomotors that reached the second half of the phantom (sectors B to D) at *t* = 25 min was higher in the presence of urea (24%) than in water (18%). A similar trend was observed for ^{124}I-nanomotors (fig. S11).

These differences increased when the mobility was limited by introducing complex paths (phantoms ii to iv). Figure 4 (C to E) shows that nanomotors reach sectors B to D much faster in urea than in water, which was confirmed by the amount of nanomotors reaching the second half of the phantom at the end of the imaging session. Values of 34.2, 17.1, and 17.0% were obtained for phantoms ii to iv in urea, whereas values in water were as low as 8.5, 4.2, and 2.1%. Equivalent results were obtained for ^{124}I-nanomotors (fig. S12), where the fractions of radioactivity in the second half of the phantom at the end of the study were 7.4, 4.2, and 2.0% for phantoms ii to iv in water, whereas values in urea were 38.2, 20.6, and 27.0%, respectively. Small differences in the values obtained using the two radionuclides might be due to inherent limitations of PET imaging. The diameter of the channels is very close to the spatial resolution of our PET imaging system, which is 1.2-mm full-width half maximum for ^{18}F, and notably lower for ^{124}I, which has less favorable emission properties (*63*). This, together with the presence of a high concentration of radioactivity in small volumes, can lead to a partial volume effect, thus causing some error in the absolute quantification values. Despite this limitation, PET imaging results unambiguously confirmed the enhanced mobility of enzyme-powered nanomotors in urea, with an effect that becomes more relevant when the complexity of the path increases.

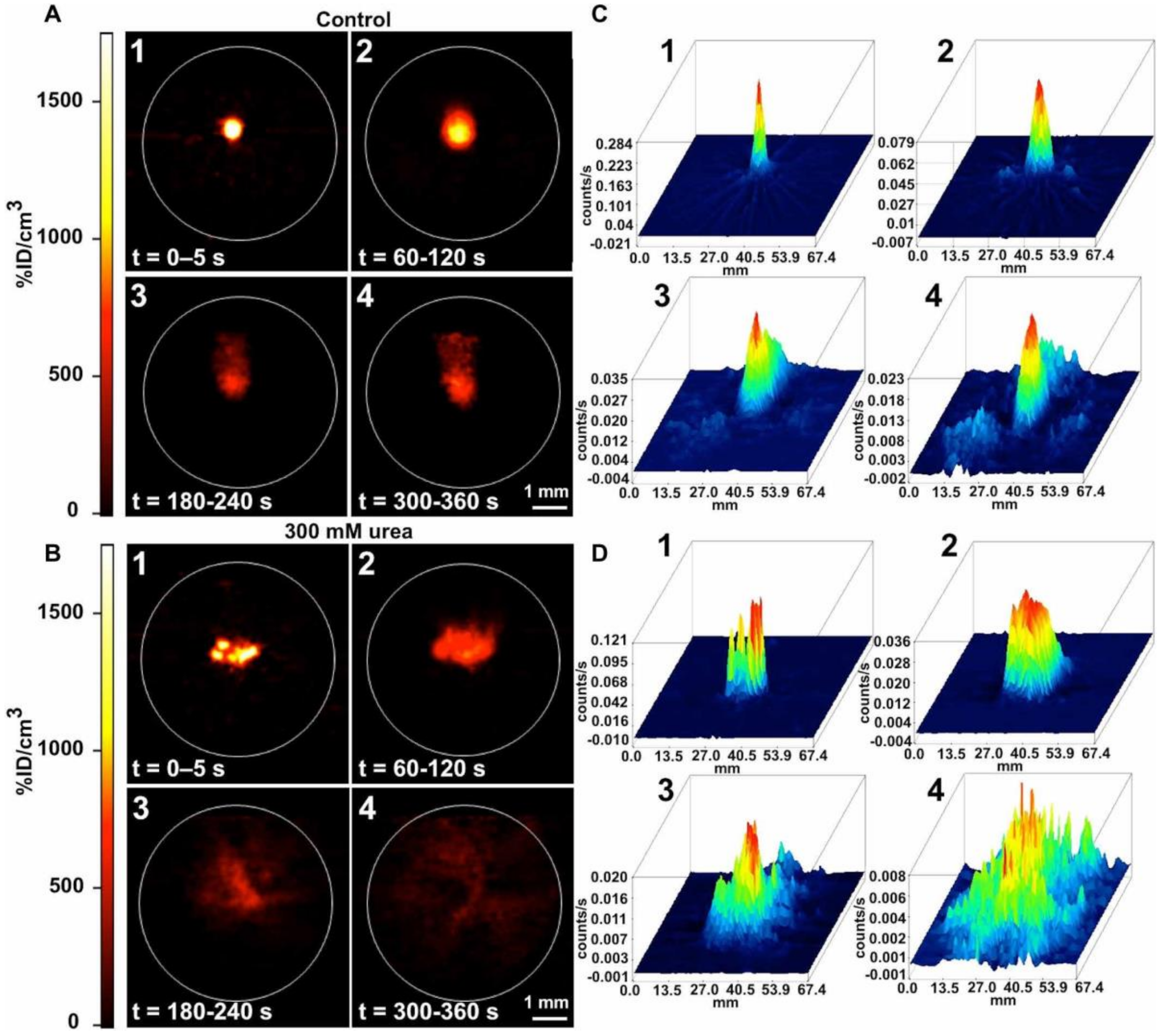

Fig. 3. In vitro imaging of urease-powered ^{18}F-nanomotor swarms by PET. Snapshots of a population of urease-powered nanomotors in (**A**) water and (**B**) 300 mM urea imaged by PET. Pixel intensity distribution histograms of the population of nanomotors in the field of view in (**C**) water and (**D**) 300 mM urea.

A biodistribution study of ^{18}F-nanomotors and ^{124}I-nanomotors in female mice after intravenous administration was carried out to (i) demonstrate the suitability of in vivo PET imaging to quantitatively track the nanomotors at the whole-body level and (ii) evaluate their radiochemical stability in vivo. Images obtained after administration of ^{18}F-nanomotors (Fig. 5A and movie S8) show a biodistribution profile with an initial accumulation in the lungs and the liver and a progressive elimination of the radioactivity via urine, as confirmed by image quantification (Fig. 5, B and C). These results suggest a rapid uptake by the mononuclear phagocyte system, as typically observed with intravenously administered nanoparticles of this size (*64*). Because the nanomotors are above the estimated size threshold for glomerular filtration (~8 nm) (*65*), the increase in radioactivity in urine indicates a slow detachment of the radiolabel from the nanomotors.

^{124}I-nanomotors also show initial accumulation in the liver and the lungs (fig. S13 and movie S8). The concentration of radioactivity in both organs progressively decreases afterward, paralleled by an increase in the thyroid gland, stomach, and urine (fig. S13, B to D). The thyroid gland and bladder are the metabolic sites of free iodine, and hence, this suggests fast nanomotor deiodination, explained by the desorption of ^{124}I from the gold surface.

Together, these results demonstrate that positron emitter–labeled nanomotors can be tracked in vivo after administration into living organisms using PET and that ^{18}F-radiolabeling yields higher radiochemical stability in vivo than ^{124}I-radiolabeling, because the detachment of the radiolabel is almost negligible over the duration of the study. No adverse effects were observed in the animals for 2 weeks after imaging sessions, thus suggesting that the administered dose is below the maximum tolerated dose.

Envisioning bladder cancer imaging and therapy and because the nanomotors' size prevents accumulation in the bladder after intra

Fig. 4. Effect of complex paths on the in vitro motion of ^{18}F-radiolabeled urease-powered nanomotors studied by PET-CT imaging. (**A**) Scheme depicting the fabrication process of 3D phantoms with different complex geometries (steps 1 to 4) and the corresponding method of analysis; (**B** to **E**) on the left, PET images (coronal projections) obtained at 0.5, 7, and 25 min after seeding of the nanomotors in different-shaped phantoms [(i) straight, (ii) rectangular, (iii) curved, and (iv) a curved path with longer straight trenches]. Scale bars, 3 mm. For each phantom, one of the channels was filled with water (left), and another channel was filled with 300 mM urea solution (right). The channels were positioned horizontally. Quantitative results of the normalized concentration of radioactivity for each sector as a function of time are shown on the right

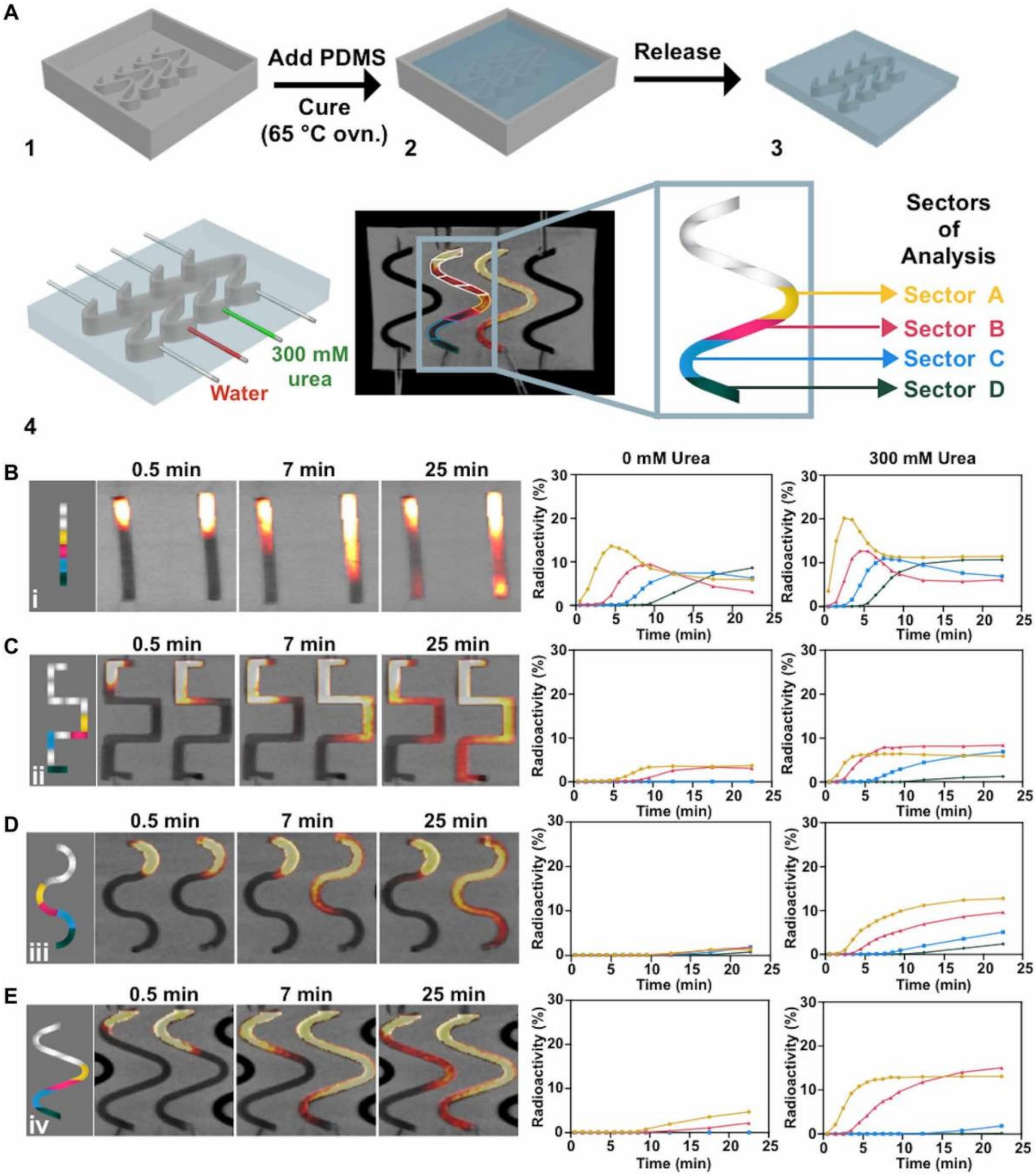

venous injection, we studied their behavior after intravesical instillation (Fig. 6). This administration route is well established in bladder cancer therapy, because it maximizes the concentration of the drug in the target organ, resulting in improved efficacy and fewer side effects (*66*).

Owing to the stability of the ^{18}F-radiolabel, demonstrated during the biodistribution study, only ^{18}F-nanomotors were used in these experiments. In addition, the use of ^{18}F should facilitate clinical translation, because it can be easily produced in biomedical cyclotrons

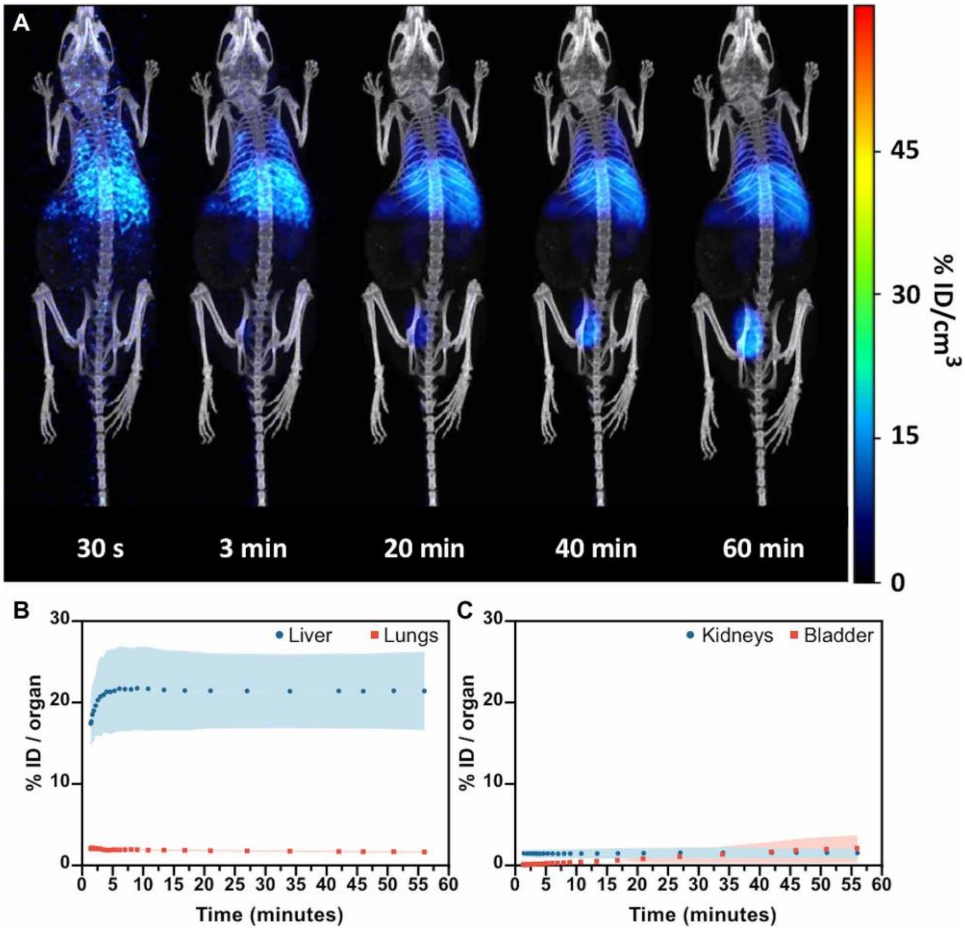

Fig. 5. Analysis of the biodistribution of ^{18}F-labeled urease-AuNP nanomotors injected intravenously in female mice. (**A**) PET-CT images (maximum intensity projections, coronal views) obtained at different time points after intravenous administration of ^{18}F-labeled urease-AuNP nanomotors; (**B**) time-activity curves in the liver and lungs and (**C**) kidneys and bladder, as determined by PET imaging. Results are expressed as percentage of injected dose per organ (mean ± SD, *N* = 2)

show a progressively divergent trend [Fig. 6C(2)], confirming that the concentration of radioactivity in the bladder was not homogeneous by the end of the study. We hypothesize that immediately after nanomotor instillation into the empty bladders, fresh urine starts entering. This (radioactivity-free) urine displaces and presents superior physical properties. When ^{18}F-nanomotors were intravesically instilled using 300 mM urea in water as the the solution present in the bladder (containing the labeled nanosystems) and two different phases are formed. Because ^{18}F-nanomotor swarms can actively move and enhance mixing in urea, they reverse the phase separation. However, when instilled in water, the separation of the two phases prevents the nanomotors from being in close contact with the urea (present only in the fresh urine), and consequently, the nanomotors lack motility, thus maintaining the phase separation. The observed phenomenon is potentially advantageous in the design of active drug delivery systems, where homogeneous distribution of the delivery vehicles is required to ensure they reach the target site.

DISCUSSION

As an additional proof of our hypothesis, we administered ^{18}F-labeled bovine serum albumin (BSA)–modified particles (MSNP-^{18}F-BSA), which do not show self-propelling properties in urea or water. In this case, the time-activity curves followed the same trend as for ^{18}F-nanomotors instilled in water (Fig. 6, B and C) (*3*, *4*), confirming that the lack of particle motility in nonhomogenization of the two phases had formed in the bladder cavity.

vehicle, we observed a uniform distribution of the radioactivity immediately after instillation, followed by a two-phase formation at *t* = 15 min [Fig. 6B(1) and movie S9]. Unexpectedly, a progressive cancelation of the difference between the two phases was observed at longer times, leading to a uniform distribution of radioactivity at *t* = 45 min. On the contrary, when administered in water, the phase separation was maintained [Fig. 6B(2)]. These observations were further confirmed by analysis of the concentration of radioactivity in two volumes of interest (VOIs) drawn within the two phases observed. For ^{18}F-nanomotors injected in urea, the time-activity profile [Fig. 6C(1)] shows that the concentration of radioactivity in both regions was close to 50% immediately after instillation (homogeneous distribution). The value in VOI 1 progressively increased to reach a maximum at ~1000 s and decreased afterward to recover starting values at $t > 2000$ s, confirming that the concentration of radioactivity within the bladder had regained homogeneity. In contrast, time-activity curves obtained under the control condition We designed AuNP-decorated enzyme-powered nanomotors and investigated their swarming behavior in vitro, both using optical microscopy and by PET-CT. When swimming without boundaries, we observed that the nanomotor swarms lead to the formation of vortices and unstable fronts and that this emergent collective behavior induces enhanced fluid convection and mixing. Moreover, when the nanomotors are subjected to boundaries in the form of complex geometries, the collective motion allows them to overcome the hurdles encountered, i.e., the turns and angles present on the paths and reach the end of the track.

We studied the suitability of PET-CT to image nanomotors in vivo and at the whole-body level, using two different radiolabeling strategies: (i) attach ^{124}I isotope to the AuNPs and (ii) directly label the enzymes with ^{18}F isotope. We not only demonstrated that PETCT is a highly adequate technique to image nanomotors but also that the direct labeling of enzymes affords a radiochemically stable structure.

Envisioning the application of urease-powered nanomotors in the treatment of bladder diseases, we studied their motility within the bladder of mice, verifying that the swarming behavior and

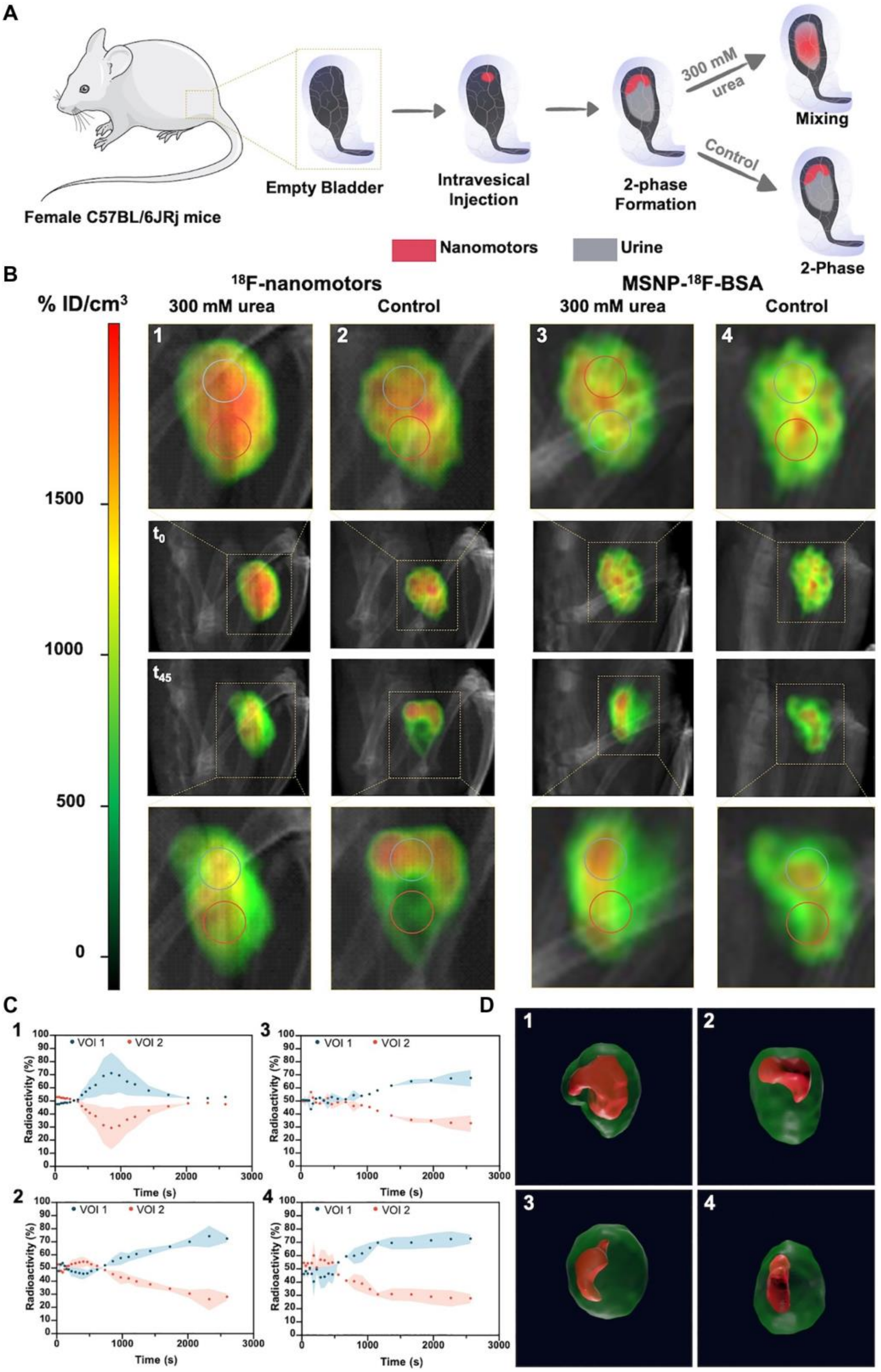
A
Female C57BL/6JRj mice
Empty Bladder
Intravesical Injection
2-phase Formation
300 mM urea
Mixing
Control
2-Phase
Nanomotors
Urine
B
% ID/cm3
18F-nanomotors
MSNP-18F-BSA
300 mM urea
Control
300 mM urea
Control
1
2
3
4
1500
1000
500
0
t0
t45
C
1
2
3
4
VOI 1
VOI 2
Radioactivity (%)
Time (s)
0
1000
2000
3000
0
10
20
30
40
50
60
70
80
90
100
D
1
2
3
4

Fig. 6. PET-CT analysis of the biodistribution in the bladder of ^{18}F-nanomotors and MSNP-18F-BSA administered via intravesical instillation. (**A**) Scheme depicting the administration method and phenomena observed. (**B**) PET-CT images (maximum intensity projections) obtained at different time points after the intravesical instillation of ^{18}F-labeled urease nanomotors in urea (1) and water (2), and control BSA-18F-MSNP in urea (3) and water (4). (**C**) Quantification analysis of the radioactivity detected

within the VOIs indicated in the PET-CT images. (**D**) 3D-reconstructed rendering of PET images of bladders showing the contour of the bladder (as a semitransparent green layer) and the regions of high intensity in PET images (as rendered red surfaces) at *t* = 45 min after administration. Same threshold levels have been set for all images.

dynamic distribution of enzymatic nanomotors also occurred in vivo. When intravesically instilled in mice, the nanomotors were able to move in swarms and exhibit enhanced fluid mixing, which led to their homogeneous distribution in the whole bladder cavity. In contrast, passive particles resulted in a nonhomogeneous distribution, where a two-phase distribution was observed.

In conclusion, we studied the collective behavior of enzymatic nanomotors in vitro and in vivo by a combination of optical microscopy and PET-CT imaging techniques. The swarming behavior and fluid mixing of enzyme nanobots observed upon intravesical injection hold great potential toward biomedical applications, where their active homogeneous distribution and enhanced fluid mixing could be exploited for targeting and drug delivery purposes. Further understanding on the mechanism of swarming formation should be addressed in the near future, from a fundamental point of view and toward a better control of pattern formation.

MATERIALS AND METHODS

Materials

Ethanol (99%), methanol (99%), hydrochloric acid (37% in water), ammonium hydroxide (25% in water), tetraethylorthosilicate (TEOS; 99%), triethanolamine (TEOA; 99%), cetyltrimethylammonium bromide (CTAB; 99%), 3-APTES (99%), GA (25% in water), urease (from *Canavalia ensiformis*, type IX, powder, 50,000 to 100,000 U/g of solid), urea (99.9%), BSA (lyophilized powder) gold(III) chloride trihydrate ($HauCl_4$), sodium citrate (NaCit), and HS-PEG5K-NH_2 (HCl salt) were purchased from Sigma-Aldrich. PBSs were purchased from Thermo Fisher Scientific. Standard Grey V4 resin (FLGPGR04) for the 3D printing of rigid molds was purchased at FormLabs. SYLGARD 184 Silicone Elastomer was purchased from Ellsworth Adhesives Ibérica.

Instruments

TEM images were captured using a JEOL JEM-2100 microscope. Hydrodynamic radii and electrophoretic mobility measurements were performed using a Wyatt Möbius. Optical videos were recorded using an inverted optical microscope (Leica DMi8) equipped with a 2.5× objective. The molds for the phantoms were fabricated by using a stereolithography 3D printer FormLabs 2 (FormLabs). The fluorine radionucleotide was synthesized using a TRACERlab FX-FN from GE Healthcare. The molecular imaging experiments were performed using a MOLECUBES □-CUBE (PET) and the MOLECUBES X-CUBE (CT) scanner.

Animals

Female mice (C57BL/6JRj, 8 weeks old, Janvier Labs; 16 animals, see below for number of animals under different experimental scenarios) weighing 20 ± 3 g were used to conduct the biodistribution studies. The animals were maintained and handled in accordance with the Guidelines for Accommodation and Care of Animals (European Convention for the Protection of Vertebrate Animals Used for Experimental and Other Scientific Purposes) and internal guidelines. All experimental procedures were approved by the ethical committee and the local authorities before conducting experimental work (code: PRO-AE-SS-059).

Synthesis of MSNPs

The MSNPs that serve as chassis for the fabrication of the nanomotors were synthesized by sol-gel chemistry using a modification of the Stöber method (*45*). Briefly, a mixture of TEOA (35 g), Milli-Q water (20 ml), and CTAB (570 mg) was placed in a three-mouthed round-bottom flask and heated up to 95°C in a silicon oil bath, under reflux and stirring, for 30 min. After this, TEOS (1.5 ml) was added dropwise. The reaction took place for 2 hours, under stirring and reflux at 95°C, and then the resulting MSNPs were collected by centrifugation (three times, 1350*g*, 5 min). The CTAB was then removed by reflux in acidic methanol. For this, the MSNPs were suspended in a methanol (30 ml) and hydrochloric acid (1.8 ml) mixture, placed in a one-mouthed round-bottom flask in a silicon oil bath at 80°C, and refluxed for 24 hours. Last, the MSNPs were collected by centrifugation and washed thrice in ethanol and thrice in Milli-Q water (three times, 1350*g*, 5 min). The concentration of the final dispersion was evaluated by dry weighing.

Amine modification of MSNPs

The surface of the MSNPs was then modified to carry free amine groups, using a modification of a reported method (*46*). Briefly, a suspension of MSNPs (2 mg/ml) in water was placed in a round-bottom flask and heated up to 50°C under vigorous stirring. Then, APTES was added to the dispersion to a final concentration of 5 mM. The reaction took place under reflux, at 50°C, for 24 hours, after which point the MSNP-NH_2s were collected and washed thrice in water by centrifugation (three times, 1350*g*, 5 min). The concentration of the final dispersion was evaluated by dry weighing.

Synthesis of AuNPs

The AuNPs were synthesized according to a previously reported method (*67*, *68*). Briefly, all necessary materials were cleaned using freshly prepared aqua regia and then rinsed extensively with water and dried in air. Then, a solution of 1 mM $HAuCl_4$ was heated up to a boil under stirring, in a round-bottom flask integrated in a reflux system. After this, 10 ml of a NaCit solution (38.8 mM) were added, and the solution was boiled for 20 min, turning red in color. The solution was stirred without heating for 1 hour, reaching room temperature. The resulting AuNP dispersion was stored at room temperature in the dark. The *Z*-potential of the synthesized AuNPs in water was −40.26 ± 2.23 mV, and their hydrodynamic radii were 10.4 ± 0.1 nm (*n* = 10).

Fabrication of nanomotors

The MSNP-NH_2s were resuspended in PBS 1× at a concentration of 1 mg/ml and a total volume of 900 □l and activated with GA (100 □l). The reaction took place for 2.5 hours, at room temperature, under mixing in an end-to-end shaker. After this, the activated MSNP-NH$_2$s were collected and washed in PBS 1× thrice by centrifugation (1350*g*, 5 min), lastly being resuspended in a solution of urease (3 mg/ml) and heterobifunctional PEG (1 μg PEG/mg of MSNP-NH$_2$) in PBS 1×. This mixture was left reacting in an end-to-end shaker for 24 hours at room temperature. The resulting nanomotors were then collected and washed three times in PBS 1× by centrifugation (1350*g*, 5 min). Then, these nanomotors were resuspended in a dispersion of AuNPs and left rotating in an end-to-end shaker for 10 min, followed by thorough washing by centrifugation (five times, 1350*g*, 5 min).

DLS and electrophoretic mobility characterization of nanomotors

A Wyatt Möbius DLS was used to characterize the hydrodynamic size distribution and surface charge of the MSNPs, MSNP-NH$_2$, GA- activated MSNP-NH$_2$, nanomotors, and AuNP-decorated nano motors.

The equipment comprises a 532-nm wavelength and a detector angle of 163.5°, and it is able to analyze for light scattering and electrophoretic mobility simultaneously. We analyzed each of the particle types at a concentration of 20 μg/ml, with an acquisition time of 5 s and three runs per experiment. A total of nine measurements per type of particle were performed to obtain statistically relevant data.

TEM imaging of the nanomotors

The AuNP-decorated nanomotors were diluted to a final concentration of 20 μg/ml in water, and the TEM images were captured.

Synthesis of [*$_{18}$*F]F-PyTFP

[^{18}F]F-PyTFP was synthesized following a previously described procedure, with modifications (*69*). Briefly, aqueous [^{18}F]fluoride was first trapped in an ion-exchange resin (Sep-Pak Accell Plus QMA Light) and subsequently eluted to the reactor vessel with a solution of Kryptofix K$_{2.2.2}$/K$_2$CO$_3$ in a mixture of water and acetonitrile. After azeotropic drying of the solvent, a solution of F-PyTFP (10 mg) in a mixture of *tert*-butanol and acetonitrile (4:1) was added and heated at 40°C for 15 min. The reaction mixture was then diluted with 1 ml of acetonitrile and 1 ml of water and purified by high- performance liquid chromatography (HPLC) using a Nucleosil 100-7 C18 column (Machery-Nagel, Düren, Germany) as the stationary phase and 0.1% trifluoroacetic acid (TFA)/acetonitrile (25:75) as the mobile phase at a flow rate of 3 ml/min. The desired fraction (retention time = 22 to 23 min; [^{18}F]F-PyTFP) was collected, diluted with water (25 ml) and flushed through a C18 cartridge (Sep-Pak Light, Waters) to selectively retain [^{18}F]F-PyTFP. The desired labeled specie was lastly eluted with acetonitrile (1 ml). Radiochemical purity was determined by radio-HPLC using a Mediterranean C18 column (4.6 mm by 150 mm, 5 μm) as the stationary phase and 0.1% TFA/ acetonitrile (0 to 1 min 25% acetonitrile, 9 to 12 min 90% acetonitrile, and 13 to 15 min 25% acetonitrile) as the mobile phase at a flow rate of 1.5 ml/min (retention time = 7.5 min).

Radiolabeling of AuNP-decorated nanomotors with [^{18}F]F-PyTFP

The radiofluorination of urease-gold nanomotors with ^{18}F was carried out by the reaction between the free amine groups of urease (e.g., present in lysine residues) contained at the surface of the nanomotors and [^{18}F]F-PyTFP. Briefly, 200 μl of AuNP-decorated nanomotor solution (1 mg/ml) was centrifuged during 10 min at 14,800 rpm, resuspended in PBS (10 μl, 10 mM, pH 8), and mixed with 4 μl of [^{18}F]F-PyTFP in acetonitrile (about 74 MBq). The reaction mixture was incubated at room temperature for 35 min. After incubation, the crude was diluted with water (100 μl) and purified by centrifugation (5 min, 14,800 rpm). The resulting precipitate was washed three times with water. The amounts of radioactivity in the supernatant and the precipitate were determined in a dose calibrator (CPCRC-25R, Capintec Inc., NJ, USA) and analyzed with radio–thin-layer chromatography (radio-TLC) using an iTLC-SG chromatography paper (Agilent Technologies, CA, USA) and dichloromethane and methanol (2:1) as the stationary and mobile phases, respectively. TLC plates were analyzed using a TLC reader (MiniGITA, Raytest).

Radiolabeling of BSA-MSNP with [^{18}F]F-PyTFP

The radiofluorination of BSA-AuNPs with ^{18}F was carried out following the same procedure described for AuNP-decorated nanomotors above.

Radiolabeling of AuNP-decorated nanomotors with ^{124}I

The radioiodination of urease-AuNPs was performed by incubation with [^{124}I]NaI. Briefly, 200 μl of urease-AuNP solution (1 mg/ml) diluted in 100 μl of water and 8 μl of [^{124}I]NaI (about 1L MBq) were incubated at room temperature for 30 min. After incubation, the reaction mixture was purified by centrifugation (5 min, 14,800 rpm). The resulting precipitate was washed three times with water (100 μl). The amounts of radioactivity in the supernatant and the precipitate were determined in a dose calibrator (CPCRC-25R, Capintec Inc., NJ, USA) and analyzed with radio-TLC, using an iTLC-SG chromatography paper (Agilent Technologies, CA, USA) and dichloromethane and methanol (2:1) as the stationary and mobile phases, respectively. TLC plates were analyzed using a TLC reader (MiniGITA, Raytest).

Optical video recording

The optical videos of the swarms of nanomotors were acquired using a Leica DMi8 microscope, coupled with a Hamamatsu high-speed cooled charge-coupled device camera and a 2.5× objective. For this, the AuNP-decorated nanomotors were centrifuged and resuspended in 200 μl of either water or PBS 1×. Then, a Petri dish was filled with 3 ml of either pure water, PBS, or a 300 mM solution of urea (in water or PBS) and placed in the microscope. A drop of 5 μl of the nanomotors was then added to the liquid-filled Petri dish, and 2-min videos were acquired at a frame rate of 25 frames per second.

Histogram analysis

The acquired videos were then analyzed for pixel intensity distribution. For this, an ROI was selected, satisfying conditions such that it enclosed both a part of the nanomotor population but also a portion of the background and a dimension of 300 pixels by

300 pixels. After this, the pixel intensity distribution within the ROI was analyzed at 12-s intervals, using ImageJ software.

Density map analysis

The density maps of the optical videos were obtained using a custom- made Python code. Before this, the videos were treated to remove the background using ImageJ software, and the grayscale images were inverted. Then, the sum of pixel intensity of blocks of 1000 frames was calculated, and the resulting images were loaded in the Python code, applying the look-up table turbo (*70*).

PIV analysis

The PIV analysis of the optical videos was performed using a custom- made Python code based on the OpenPIV library. Before loading the images in the code, the frames of the videos were treated to remove the background using ImageJ software. After this, the resulting images were loaded in the Python code, with a window size of 24 pixels, a window overlap of 3 pixels, a search size of 25 pixels, and a frame rate of 0.4 s. Spurious vectors were removed by applying local, global, and signal-to-noise ratio filters.

Phantom fabrication

To analyze the effect of complex paths on the motility of passive nanoparticles and active nanomotor swarms, phantoms with different shapes were fabricated. To obtain the desired channels' geometry, a 3D design was prepared by using autoCAD software and posttreated with PreForm Software to be later 3D printed by stereolithography. The rigid mold containing the inverse design of the desired channels was printed, followed by the required postprocessing steps: (i) removal of the nonpolymerized resin by two sequential washing steps in an isopropanol bath, (ii) hardening of the photopolymerized resin by 15 min of ultraviolet exposure, and (iii) removal of support structures. To fabricate the flexible and transparent polydimethylsiloxane (PDMS)–based channels, the catalyzer and the monomer were first mixed at a ratio of 1:10, and the solution was degassed for 15 min to avoid the bubble presence on the final chip. The solution was poured onto the rigid mold, followed by the curing process at 65°C overnight. The polymerized PDMS was then removed from the rigid mold, containing the desired channels. At this stage, the tubbing was implemented in the system, removing any debris that would fall into the channels. To close the system and obtain the phantom, a 2-mm-thick layer of flat PDMS was bound to the open side of the channels using a 2-min plasma treatment.

PET-CT image acquisition

In vitro imaging studies were conducted using PET-CT as molecular imaging techniques. All the phantoms were filled with either 300 mM urea solution in water or ultrapure water (one channel with each medium) and positioned in the center of the field of view of the MOLECUBES □-CUBE (PET) scanner. The field of view was selected to cover the whole length of the phantom. For each type of nanomotor, two samples (10 □l, about 1 MBq each) were seeded simultaneously in one of the edges of the phantom, one in the channel filled with urea solution and the other one in the channel filled with ultrapure water. Immediately after, a dynamic PET scan was acquired for 25 min, followed by a CT acquisition.

Phantom PET-CT imaging analysis

PET images were reconstructed and analyzed using PMOD image processing tool. With that aim, the whole channel was divided in sectors with the same length over the coronal view, and the concentration of activity in each section was determined as a function on time. The values of activity concentration were lastly normalized to the whole amount of radioactivity in the channel.

Intravenous administration

Anesthesia was induced by inhalation of 3% isoflurane in pure O_2 and maintained by 1.5 to 2% isofluorane in 100% O_2. With the animal under anesthesia, the F-nanomotors or I-nanomotors were injected via one of the lateral tail veins using PBS (pH 7.4) as the vehicle (*N* = 2 for each type of radiolabeling; see Table 1 for details). Dynamic, whole-body 60-min PET imaging sessions were immediately started after administration of the labeled compounds using a MOLECUBES □-CUBE scanner. After the PET scan, whole-body high-resolution CT acquisitions were performed on the MOLECUBES X-CUBE scanner to provide anatomical information of each animal and the attenuation map for the later reconstruction of the PET images.

Intravesical administration

Anesthesia was induced by inhalation of 3% isoflurane in pure O_2 and maintained by 1.5 to 2% isofluorane in 100% O_2. With the animal under anesthesia, the animals were positioned in supine position, and the bladder was emptied by massaging the abdominal region. Immediately after, the F-nanomotors and MSNP-F-BSA were introduced in the bladder (through a catheter) by intravesical administration using 300 mM urea or water as the vehicle (*N* = 2 for each type of radiolabeling and vehicle; see Table 1 for details). Administration was followed by 45-min PET imaging sessions and whole-body high-resolution CT acquisitions as above. PET images were reconstructed using 3D OSEM (ordered subset expectation maximization) reconstruction algorithm and applying random, scatter, and attenuation corrections. PET-CT images of the same mouse were coregistered and analyzed using PMOD image processing tool.

Biodistribution analysis

VOIs were placed on selected organs (namely, brain, thyroid, lungs, liver, stomach, kidneys, spleen, and bladder), as well as the heart to get an estimation of the concentration of radioactivity in blood. Time-activity curves (decay corrected) were obtained as cps/cm^3 in each organ. Curves were transformed into real activity (Bq/cm^3) curves by using a calibration factor, obtained from previous scans performed on a phantom (Micro Deluxe, Data Spectrum Corp.) under the same experimental conditions (isotope, reconstruction algorithm, and energetic window).

Bladder distribution analysis

PET images were reconstructed using 3D OSEM reconstruction algorithm and applying random, scatter, and attenuation corrections. PET-CT images of the same mouse were coregistered and analyzed using PMOD image processing tool. Two VOIs were placed on the upper and lower regions of the bladder (namely, VOI 1 and VOI 2) to obtain the concentration of radioactivity in both VOIs over time. The values were normalized to the maximum values for each frame.

For the generation of 3D-rendered images of the bladder, raw 16-bit PET images (pixel values from 0 to 65,546) were imported into ImageJ software and color coded. Images were resized by a factor of 3 in all three dimensions using bilinear interpolation. Pixels with a value below 5000 were removed as noise, and orthogonal cuts through the object (axial, coronal, and sagittal) were created using the Orthogonal Views function of ImageJ. For 3D rendering, raw 16-bit PET images (pixel values from 0 to 65,546) were opened in ImageJ and resized threefold (bilinear interpolation), and two copies of each image were created, one including all pixels above a value of 5000 (all but noise, corresponding to the whole bladder contour) and another with pixels with values above 45,000 (high-intensity regions in PET). Both images were transformed in binary masks, rendered as surfaces, and exported as STL (Standard Triangle Language) files using ImageJ 3D-viewer plug-in. STL files were imported into Blender 2.8 and beautified by giving a semitransparent aspect to image 1 (bladder contour) and a solid aspect to image 2 (high-intensity regions). Point of view and illumination of the scene were manually selected for each set of images, and 2D images presented here were rendered.

Table 1. Summary of the in vivo studies performed with the different types of nanomotors and administration routes.

Group	Number of animals	Particle	Administration route	Vehicle	Activity (MBq)	Mass of particles (g)
1	2	F-nanomotors	Intravenous	PBS	2.2 ± 0.10	73
2	2	I-nanomotors	Intravenous	PBS	1.6 ± 0.10	73
3	2	F-nanomotors	Intravesical	Water	1.6 ± 0.10	33
4	2	F-nanomotors	Intravesical	Urea	1.9 ± 0.15	33
5	2	MSNP-F-BSA	Intravesical	Water	0.5 ± 0.06	33
6	2	MSNP-F-BSA	Intravesical	Urea	0.4 ± 0.05	33

SUPPLEMENTARY MATERIALS

robotics.sciencemag.org/cgi/content/full/6/52/eabd2823/DC1 Fig.
S1. Characterization of the AuNP-decorated nanomotors.
Fig. S2. Motion analysis of single urease-powered nanomotors.
Fig. S3. In vitro imaging of urease-powered nanomotor swarms by optical microscopy.
Fig. S4. In vitro imaging of urease-powered nanomotor swarms by optical microscopy.
Fig. S5. In vitro imaging of urease-powered nanomotor swarms by optical microscopy. Fig.
S6. In vitro analysis of the motion of swarms of urease-powered AuNP-decorated nanomotors by optical microscopy.
Fig. S7. Motion analysis of the nanomotor swarms by optical microscopy.
Fig. S8. Analysis of large passive MSNP (without enzymes) populations. Fig. S9.
Motion analysis of the nanomotor swarms codropped with 5-m PS tracer microparticles [0.01% (w/v)] in water.
Fig. S10. Motion analysis of the nanomotor swarms codropped with 5-m PS tracer microparticles [0.01% (w/v)] in PBS.
Fig. S11. Fabrication of the molds for the complex paths phantoms.
Fig. S12. PET-CT coronal images obtained a 0.5, 7, and 25 min for each phantom, which was filled with either Milli-Q water or 300 mM urea solution.
Fig. S13. Analysis of the biodistribution of I-nanomotors injected intravenously. Fig. S14.
Image sets showing the PET images of the different bladders just after injection of nanomotors (*t* = 0) and 45 min later.
Movie S1. Motion of single nanomotor in water and in PBS.
Movie S2. In vitro imaging of enzyme-powered nanomotor swarms in water by optical microscopy. Movie S3. In vitro imaging of enzyme-powered nanomotor swarms in PBS by optical microscopy.
Movie S4. In vitro imaging of passive MSNPs dropped onto water and water-based urea solutions by optical microscopy.
Movie S5. In vitro imaging of enzyme-powered nanomotor swarms and tracer microparticles in water and in PBS by optical microscopy.
Movie S6. In vitro imaging of enzyme-powered nanomotor swarms by PET.
Movie S7. Effect of complex paths on the in vitro motion of ^{18}F-radiolabeled urease-powered nanomotors studied by PET-CT imaging.
Movie S8. Study of the biodistribution of enzyme-powered nanomotors by PET-CT. Movie
S9. PET-CT analysis of the distribution of ^{18}F-nanomotors and MSNP-^{18}F-BSA in the bladder administered via intravesical instillation.

REFERENCES AND NOTES

1. S. Wilhelm, A. J. Tavares, Q. Dai, S. Ohta, J. Audet, H. F. Dvorak, W. C. W. Chan, Analysis of nanoparticle delivery to tumours. *Nat. Rev. Mater.* **1**, 16014 (2016).
2. Z. Wu, X. Lin, Y. Wu, T. Si, J. Sun, Q. He, Near-infrared light-triggered "on/off" motion of polymer multilayer rockets. *ACS Nano* **8**, 6097–6105 (2014).
3. S. M. Douglas, I. Bachelet, G. M. Church, A logic-gated nanorobot for targeted transport of molecular payloads. *Science* **335**, 831–834 (2012).
4. A. C. Hortelão, R. Carrascosa, N. Murillo-Cremaes, T. Patiño, S. Sánchez, Targeting 3D bladder cancer spheroids with urease-powered nanomotors. *ACS Nano* **13**, 429–439 (2019).
5. F. Hallouard, N. Anton, P. Choquet, A. Constantinesco, T. Vandamme, Iodinated blood pool contrast media for preclinical X-ray imaging applications—A review. *Biomaterials* **31**, 6249–6268 (2010).
6. A. C. Hortelão, T. Patiño, A. Perez-Jiménez, À. Blanco, S. Sánchez, Enzyme-powered nanobots enhance anticancer drug delivery. *Adv. Funct. Mater.* **28**, 1705086 (2018).
7. F. Peng, Y. Tu, D. A. Wilson, Micro/nanomotors towards: In vivo application: Cell, tissue and biofluid. *Chem. Soc. Rev.* **46**, 5289–5310 (2017).
8. A. Llopis-Lorente, A. Garciá-Fernández, N. Murillo-Cremaes, A. C. Hortelaõ, T. Patinõ, R. Villalonga, F. Sancenón, R. Martínez-Máñez, S. Sánchez, Enzyme-powered gated mesoporous silica nanomotors for on-command intracellular payload delivery. *ACS Nano* **13**, 12171–12183 (2019).
9. S. Tang, F. Zhang, H. Gong, F. Wei, J. Zhuang, E. Karshalev, B. Esteban-Fernández de Ávila, C. Huang, Z. Zhou, Z. Li, L. Yin, H. Dong, R. H. Fang, X. Zhang, L. Zhang, J. Wang, Enzyme-powered Janus platelet cell robots for active and targeted drug delivery. *Sci. Robot.* **5**, eaba6137 (2020).
10. W. Gao, R. Dong, S. Thamphiwatana, J. Li, W. Gao, L. Zhang, J. Wang, Artificial micromotors in the mouse's stomach: A step toward in vivo use of synthetic motors. *ACS Nano* **9**, 117–123 (2015).
11. D. Schamel, A. G. Mark, J. G. Gibbs, C. Miksch, K. I. Morozov, A. M. Leshansky, P. Fischer, Nanopropellers and their actuation in complex viscoelastic media. *ACS Nano* **8**, 8794–8801 (2014).
12. H. Choi, S. H. Cho, S. K. Hahn, Urease-powered polydopamine nanomotors for intravesical therapy of bladder diseases. *ACS Nano* **14**, 6683–6692 (2020).
13. D. Walker, B. T. Kasdorf, H.-H. Jeong, O. Lieleg, P. Fischer, Enzymatically active biomimetic micropropellers for the penetration of mucin gels. *Sci. Adv.* **1**, e1500501 (2015).
14. J. Wang, B. J. Toebes, A. S. Plachokova, Q. Liu, D. Deng, J. A. Jansen, F. Yang, D. A. Wilson, Self-propelled PLGA micromotor with chemotactic response to inflammation. *Adv. Healthc. Mater.* **9**, 1901710 (2020).
15. F. Peng, Y. Tu, A. Adhikari, J. C. J. Hintzen, D. W. P. M. Löwik, D. A. Wilson, A peptide functionalized nanomotor as efficient cell penetrating tool. *Chem. Commun.* **53**, 1088–1091 (2016).
16. J. Sun, M. Mathesh, W. Li, D. A. Wilson, Enzyme-powered nanomotors with controlled size for biomedical applications. *ACS Nano* **13**, 10191–10200 (2019).
17. M. A. Ramos-Docampo, M. Fernández-Medina, E. Taipaleenmäki, O. Hovorka, V. Salgueiriño, B. Städler, Microswimmers with heat delivery capacity for 3D cell spheroid penetration. *ACS Nano* **13**, 12192–12205 (2019).
18. G. von Maltzahn, J.-H. Park, K. Y. Lin, N. Singh, C. Schwöppe, R. Mesters, W. E. Berdel, E. Ruoslahti, M. J. Sailor, S. N. Bhatia, Nanoparticles that communicate in vivo to amplify tumour targeting. *Nat. Mater.* **10**, 545–552 (2011).

19. D. Needleman, Z. Dogic, Active matter at the interface between materials science and cell biology. *Nat. Rev. Mater.* **2**, 17048 (2017).
20. M. Whiteley, S. P. Diggle, E. P. Greenberg, Progress in and promise of bacterial quorum sensing research. *Nature* **551**, 313–320 (2017).
21. K. Kawabata, M. Nagayama, H. Haga, T. Sambongi, Mechanical effects on collective phenomena of biological systems: Cell locomotion. *Curr. Appl. Phys.* **1**, 66–71 (2001).
22. Z.-M. Qian, S. H. Wang, X. E. Cheng, Y. Q. Chen, An effective and robust method for tracking multiple fish in video image based on fish head detection. *BMC Bioinformatics* **17**, 251 (2016).
23. Z. Deng, F. Mou, S. Tang, L. Xu, M. Luo, J. Guan, Swarming and collective migration of micromotors under near infrared light. *Appl. Mater. Today* **13**, 45–53 (2018).
24. X. Yan, Q. Zhou, M. Vincent, Y. Deng, J. Yu, J. Xu, T. Xu, T. Tang, L. Bian, Y.-X. J. Wang, K. Kostarelos, L. Zhang, Multifunctional biohybrid magnetite microrobots for imagingguided therapy. *Sci. Robot.* **2**, eaaq1155 (2017).
25. A. Somasundar, S. Ghosh, F. Mohajerani, L. N. Massenburg, T. Yang, P. S. Cremer, D. Velegol, A. Sen, Positive and negative chemotaxis of enzyme-coated liposome motors. *Nat. Nanotechnol.* **14**, 1129–1134 (2019).
26. Z. Wu, L. Li, Y. Yang, P. Hu, Y. Li, S.-Y. Yang, L. V. Wang, W. Gao, A microrobotic system guided by photoacoustic computed tomography for targeted navigation in intestines in vivo. *Sci. Robot.* **4**, eaax0613 (2019).
27. A. Aubret, M. Youssef, S. Sacanna, J. Palacci, Targeted assembly and synchronization of self-spinning microgears. *Nat. Phys.* **14**, 1114–1118 (2018).
28. C. Zhou, N. J. Suematsu, Y. Peng, Q. Wang, X. Chen, Y. Gao, W. Wang, Coordinating an ensemble of chemical micromotors via spontaneous synchronization. *ACS Nano* **14**, 5360–5370 (2020).
29. X. Chen, C. Zhou, Y. Peng, Q. Wang, W. Wang, Temporal light modulation of photochemically active, oscillating micromotors: Dark pulses, mode switching, and controlled clustering. *ACS Appl. Mater. Interfaces* **12**, 11843–11851 (2020).
30. X. Cao, E. Panizon, A. Vanossi, N. Manini, C. Bechinger, Orientational and directional locking of colloidal clusters driven across periodic surfaces. *Nat. Phys.* **15**, 776–780 (2019).
31. D. Zhou, Y. Gao, J. Yang, Y. C. Li, G. Shao, G. Zhang, T. Li, L. Li, Light-ultrasound driven collective “firework” behavior of nanomotors. *Adv. Sci.* **5**, 1800122 (2018).
32. F. Mou, X. Li, Q. Xie, J. Zhang, K. Xiong, L. Xu, J. Guan, Active micromotor systems built from passive particles with biomimetic predator-prey interactions. *ACS Nano* **14**, 406–414 (2020).
33. T. Xu, F. Soto, W. Gao, R. Dong, V. Garcia-Gradilla, E. Magaña, X. Zhang, J. Wang, Reversible swarming and separation of self-propelled chemically powered nanomotors under acoustic fields. *J. Am. Chem. Soc.* **137**, 2163–2166 (2015).
34. M. Ibele, T. E. Mallouk, A. Sen, Schooling behavior of light-powered autonomous micromotors in water. *Angew. Chemie Int. Ed.* **48**, 3308–3312 (2009).
35. J. Yan, M. Han, J. Zhang, C. Xu, E. Luijten, S. Granick, Reconfiguring active particles by electrostatic imbalance. *Nat. Mater.* **15**, 1095–1099 (2016).
36. I. Buttinoni, J. Bialké, F. Kümmel, H. Löwen, C. Bechinger, T. Speck, Dynamical clustering and phase separation in suspensions of self-propelled colloidal particles. *Phys. Rev. Lett.* **110**, 238301 (2013).
37. T. Bäuerle, A. Fischer, T. Speck, C. Bechinger, Self-organization of active particles by quorum sensing rules. *Nat. Commun.* **9**, 3232 (2018).
38. J. Palacci, S. Sacanna, A. P. Steinberg, D. J. Pine, P. M. Chaikin, Living crystals of lightactivated colloidal surfers. *Science* **339**, 936–940 (2013).
39. J. Yu, D. Jin, K.-F. Chan, Q. Wang, K. Yuan, L. Zhang, Active generation and magnetic actuation of microrobotic swarms in bio-fluids. *Nat. Commun.* **10**, 5631 (2019).
40. Z. Wu, J. Troll, H.-H. Jeong, Q. Wei, M. Stang, F. Ziemssen, Z. Wang, M. Dong, S. Schnichels, T. Qiu, P. Fischer, A swarm of slippery micropropellers penetrates the vitreous body of the eye. *Sci. Adv.* **4**, eaat4388 (2018).
41. A. Servant, F. Qiu, M. Mazza, K. Kostarelos, B. J. Nelson, Controlled in vivo swimming of a swarm of bacteria-like microrobotic flagella. *Adv. Mater.* **27**, 2981–2988 (2015).
42. M. Bauer, C. C. Wagner, O. Langer, Microdosing studies in humans. *Drugs R D* **9**, 73–81 (2008).
43. M. Bergstrom, The use of microdosing in the development of small organic and protein therapeutics. *J. Nucl. Med.* **58**, 1188–1195 (2017).
44. D. Vilela, U. Cossío, J. Parmar, A. M. Martínez-Villacorta, V. Gómez-Vallejo, J. Llop, S. Sánchez, Medical imaging for the tracking of micromotors. *ACS Nano* **12**, 1220–1227 (2018).
45. Q. He, X. Cui, F. Cui, L. Guo, J. Shi, Size-controlled synthesis of monodispersed mesoporous silica nano-spheres under a neutral condition. *Microporous Mesoporous Mater.* **117**, 609–616 (2009).
46. Y. Wang, Y. Sun, J. Wang, Y. Yang, Y. Li, Y. Yuan, C. Liu, Charge-reversal APTES-modified mesoporous silica nanoparticles with high drug loading and release controllability. *ACS Appl. Mater. Interfaces* **8**, 17166–17175 (2016).
47. H. Xu, F. Yan, E. E. Monson, R. Kopelman, Room-temperature preparation and characterization of poly (ethylene glycol)-coated silica nanoparticles for biomedical applications. *J. Biomed. Mater. Res. A* **66A**, 870–879 (2003).
48. M. R. Ivanov, H. R. Bednar, A. J. Haes, Investigations of the mechanism of gold nanoparticle stability and surface functionalization in capillary electrophoresis. *ACS Nano* **3**, 386–394 (2009).
49. Z. Liu, Y. Yan, F. T. Chin, F. Wang, X. Chen, Dual integrin and gastrin-releasing peptide receptor targeted tumor imaging using 18F-labeled PEGylated RGD-bombesin heterodimer 18F-FB-PEG3-Glu-RGD-BBN. *J. Med. Chem.* **52**, 425–432 (2009).
50. K. R. Pulagam, K. B. Gona, V. Gómez-Vallejo, J. Meijer, C. Zilberfain, I. Estrela-Lopis, Z. Baz, U. Cossío, J. Llop, Gold nanoparticles as boron carriers for boron neutron capture therapy: Synthesis, radiolabelling and in vivo evaluation. *Molecules* **24**, 3609 (2019).
51. X. Ma, A. Jannasch, U.-R. Albrecht, K. Hahn, A. Miguel-López, E. Schäffer, S. Sánchez, Enzyme-powered hollow mesoporous janus nanomotors. *Nano Lett.* **15**, 7043–7050 (2015).
52. X. Arqué, A. Romero-Rivera, F. Feixas, T. Patiño, S. Osuna, S. Sánchez, Intrinsic enzymatic properties modulate the self-propulsion of micromotors. *Nat. Commun.* **10**, 2826 (2019). 53. T. Patiño, N. Feiner-Gracia, X. Arqué, A. Miguel-López, A. Jannasch, T. Stumpp, E. Schäffer, L. Albertazzi, S. Sánchez, Influence of enzyme quantity and distribution on the selfpropulsion of non-janus urease-powered micromotors. *J. Am. Chem. Soc.* **140**, 7896–7903 (2018).
54. M. De Corato, X. Arqué, T. Patiño, M. Arroyo, S. Sánchez, I. Pagonabarraga, Self-propulsion of active colloids via ion release: Theory and experiments. *Phys. Rev. Lett.* **124**, 108001 (2020).
55. L. Liu, H. Mo, S. Wei, D. Raftery, Quantitative analysis of urea in human urine and serum by 1H nuclear magnetic resonance. *Analyst* **137**, 595–600 (2012).
56. L. Soler, V. Magdanz, V. M. Fomin, S. Sanchez, O. G. Schmidt, Self-propelled micromotors for cleaning polluted water. *ACS Nano* **7**, 9611–9620 (2013).
57. J. Orozco, B. Jurado-Sánchez, G. Wagner, W. Gao, R. Vazquez-Duhalt, S. Sattayasamitsathit, M. Galarnyk, A. Cortés, D. Saintillan, J. Wang, Bubble-propelled micromotors for enhanced transport of passive tracers. *Langmuir* **30**, 5082–5087 (2014).
58. E. Morales-Narváez, M. Guix, M. Medina-Sánchez, C. C. Mayorga-Martinez, A. Merkoçi, Micromotor enhanced microarray technology for protein detection. *Small* **10**, 2542–2548 (2014).
59. L. Valdez, H. Shum, I. Ortiz-Rivera, A. C. Balazs, A. Sen, Solutal and thermal buoyancy effects in self-powered phosphatase micropumps. *Soft Matter* **13**, 2800–2807 (2017).
60. I. Ortiz-Rivera, H. Shum, A. Agrawal, A. Sen, A. C. Balazs, Convective flow reversal in self-powered enzyme micropumps. *Proc. Natl. Acad. Sci. U.S.A.* **113**, 2585–2590 (2016).
61. S. Maiti, O. E. Shklyaev, A. C. Balazs, A. Sen, Self-organization of fluids in a multienzymatic pump system. *Langmuir* **35**, 3724–3732 (2019).
62. M. Alarcón-Correa, J.-P. Günther, J. Troll, V. M. Kadiri, J. Bill, P. Fischer, D. Rothenstein, Self-assembled phage-based colloids for high localized enzymatic activity. *ACS Nano* **13**, 5810–5815 (2019).
63. H. W. A. M. de Jong, L. Perk, G. W. M. Visser, R. Boellaard, G. A. M. S. van Dongen, A. A. Lammertsma, High resolution PET imaging characteristics of ^{68}Ga, ^{124}I and ^{89}Zr compared to $_{18}$F, in *IEEE Nuclear Science Symposium Conference Record, 2005* (Puerto Rico, 23 to 29 October 2005), vol. 3, pp. 1624–1627.
64. N. Hoshyar, S. Gray, H. Han, G. Bao, The effect of nanoparticle size on in vivo pharmacokinetics and cellular interaction. *Nanomedicine* **11**, 673–692 (2016).
65. B. Du, X. Jiang, A. Das, Q. Zhou, M. Yu, R. Jin, J. Zheng, Glomerular barrier behaves as an atomically precise bandpass filter in a sub-nanometre regime. *Nat. Nanotechnol.* **12**, 1096–1102 (2017).
66. S. Il Kim, S. H. Choo, *Bladder Cancer*, J. H. Ku, Ed. (Elsevier, ed. 1, 2018), pp. 263–276.
67. K. Ai, Y. Liu, L. Lu, Hydrogen-bonding recognition-induced color change of gold nanoparticles for visual detection of melamine in raw milk and infant formula. *J. Am. Chem. Soc.* **131**, 9496–9497 (2009).
68. D. Vilela, A. C. Hortelao, R. Balderas-Xicohténcatl, M. Hirscher, K. Hahn, X. Ma, S. Sánchez, Facile fabrication of mesoporous silica micro-jets with multi-functionalities. *Nanoscale* **9**, 13990–13997 (2017).
69. D. E. Olberg, J. M. Arukwe, D. Grace, O. K. Hjelstuen, M. Solbakken, G. M. Kindberg, A. Cuthbertson, One step radiosynthesis of 6-[18F]fluoronicotinic acid 2,3,5,6-tetrafluorophenyl ester ([18F]F-Py-TFP): A new prosthetic group for efficient labeling of biomolecules with fluorine-18. *J. Med. Chem.* **53**, 1732–1740 (2010).
70. A. Mikhailov, *Turbo, An Improved Rainbow Colormap for Visualization* (Google AI Blog, 2019).

Acknowledgments

Funding: The research leading to these results has received funding from the Spanish MINECO (BOTSinFluids project), the Foundation BBVA (MEDIROBOTS project), the CERCA program by the Generalitat de Catalunya, and the CaixaImpulse program by La Caixa Foundation (TERANOBOTS project). This project has received funding from the European Research Council (ERC) under the European Union’s Horizon 2020 research and innovation program (grant agreement no. 866348; iNanoSwarms). A.C.H. thanks MINECO for the Severo Ochoa PhD fellowship. M.G. thanks MINECO for the Juan de la Cierva fellowship (IJCI201630451), the Beatriu de Pinós Programme (2018-BP-00305), and the Ministry of Business and Knowledge of the Government of Catalonia. D.V. acknowledges financial support provided by the European Commission under Horizon 2020s

Marie Skłodowska-Curie Actions COFUND scheme (grant agreement no. 712754) and by the Severo Ochoa program of the Spanish Ministry of Economy and Competitiveness [grant SEV-2014-0425 (2015–2019)]. T.P. thanks the European Union's Horizon 2020 research and innovation program, under the Marie Skłodowska-Curie Individual Fellowship (H2020-MSCA-IF2018, DNA-bots). J.L. thanks the Spanish Ministry of Economy and Competitiveness (grants CTQ2017-87637-R , SAF2017-87670-R) for financial support. Part of the work was conducted under the Maria de Maeztu Units of Excellence Programme (grant no. MDM-2017-0720). **Author contributions:** A.C.H synthesized the nanomotors, performed their characterization, optical tracking, corresponding image processing, and data analysis. C.S. performed radiolabeling, PET-CT experiments, and data analysis. M.G. fabricated the phantoms and helped with graphic design and video editing. S.G.-G. and E.J. helped set up the intravesical administration model. D.V. synthesized the AuNPs and performed their characterization. L.R developed the ^{18}F-radiolabeling protocol. P.R.-C. provided graphic design of the radiochemical facility and contributed in image analysis after intravesical instillation. U.C. performed reconstruction, analysis, and quantification of PET images. V.G.-V. contributed to the in vivo experimental design. T.P., J.L., and S.S. conceived the idea, designed, and supervised the work. The manuscript was written through contributions of all authors. All authors have given approval to the final version of the manuscript. **Competing interests:** The authors declare that they have no competing interests. **Data and materials availability:** All data needed to support the conclusions of this paper are available in the paper or the Supplementary Materials.

Citation: A. C. Hortelao, C. Simó, M. Guix, S. Guallar-Garrido, E. Julián, D. Vilela, L. Rejc, P. Ramos-Cabrer, U. Cossío, V. Gómez-Vallejo, T. Patiño, J. Llop, S. Sánchez, Swarming behavior and in vivo monitoring of enzymatic nanomotors within the bladder. *Sci. Robot.* **6**, eabd2823 (2021)